






ARTICLE

<https://doi.org/10.1038/s41467-019-13406-9>

OPEN

Detection of the $5p - 4f$ orbital crossing and its optical clock transition in Pr^{9+}

H. Bekker ^{1,6}, A. Borschevsky², Z. Harman¹, C.H. Keitel¹, T. Pfeifer ¹, P.O. Schmidt ^{3,4},
J.R. Crespo López-Urrutia ¹ & J.C. Berengut ^{1,5*}

Recent theoretical works have proposed atomic clocks based on narrow optical transitions in highly charged ions. The most interesting candidates for searches of physics beyond the Standard Model are those which occur at rare orbital crossings where the shell structure of the periodic table is reordered. There are only three such crossings expected to be accessible in highly charged ions, and hitherto none have been observed as both experiment and theory have proven difficult. In this work we observe an orbital crossing in a system chosen to be tractable from both sides: Pr^{9+} . We present electron beam ion trap measurements of its spectra, including the inter-configuration lines that reveal the sought-after crossing. With state-of-the-art calculations we show that the proposed nHz-wide clock line has a very high sensitivity to variation of the fine-structure constant, α , and violation of local Lorentz invariance; and has extremely low sensitivity to external perturbations.

¹Max-Planck-Institut für Kernphysik, Saupfercheckweg 1, 69117 Heidelberg, Germany. ²Van Swinderen Institute, University of Groningen, Nijenborgh 4, 9747 AG Groningen, The Netherlands. ³Physikalisch-Technische Bundesanstalt, Bundesallee 100, 38116 Braunschweig, Germany. ⁴Institut für Quantenoptik, Leibniz Universität Hannover, Welfengarten 1, 30167 Hannover, Germany. ⁵School of Physics, University of New South Wales, NSW 2052 Kensington, Australia. ⁶Present address: Department of Physics, Columbia University, 538 West 120th Street, New York, NY 10027-5255, USA. *email: julian.berengut@unsw.edu.au

Current single ion clocks reach fractional frequency uncertainties $\delta\nu/\nu$ around 10^{-18} , and enable sensitive tests of relativity and searches for potential variations in fundamental constants^{1–5}. These experiments could be improved by exploiting clock transitions with a much reduced sensitivity to frequency shifts caused by external perturbations. Transitions in highly charged ions (HCI) naturally meet this requirement due to their spatially compact wave functions^{6,7}. Unfortunately, in most cases this raises the transition frequencies beyond the range of current precision lasers. While some forbidden fine-structure transitions remain in the optical range, these are generally insensitive to physics beyond the Standard Model. More interestingly, at configuration crossings due to re-orderings of electronic orbital binding energies along an isoelectronic sequence, many optical transitions between the nearly degenerate configurations can exist^{7,8}. For the $5p$ and $4f$ orbitals, this was predicted to occur at Sn-like Pr^{9+} , see Fig. 1. Here, the $5p^2\ ^3P_0 - 5p4f\ ^3G_3$ magnetic octupole (M3) transition seems ideally suited for an ultra-precise atomic clock and searches for physics beyond the Standard Model with HCI^{8–10}, recently reviewed in ref. 11. It is highly sensitive to potential variation of the fine-structure constant, α , and to violation of local Lorentz invariance (LLI).

With two electrons above closed shells, Pr^{9+} has a less complex electronic structure than the open $4f$ -shell systems studied in previous works^{12–14}. Nonetheless, predictions do not reach the accuracy needed for finding the clock transition in a precision laser spectroscopy experiment.

In the following, we present measurements of all the optical magnetic-dipole (M1) transitions with rates of at least order $100\ \text{s}^{-1}$ taking place between the fine-structure states of the $5p^2$ and $5p4f$ configurations. Since these configurations have both even parity, strongly mixed levels exist, allowing for relatively strong M1 transitions between them. By measuring these and applying the Rydberg-Ritz combination principle, the wavelength of the extremely weak clock transition is inferred to be $452.334(1)$

nm. Our calculations show that the proposed nHz-wide clock line, proceeds through hyperfine admixture of its upper state with an E2-decaying level. Moreover, we find that it has competitive sensitivities to physics beyond the Standard Model. These favorable properties can be exploited with the detailed experimental scheme that we propose.

Results

Measurement and identification of the lines. The Heidelberg electron beam ion trap (HD-EBIT) was employed to produce and trap Pr^{9+} ions¹⁵. In this setup, a magnetically focused electron beam traverses a tenuous beam of $\text{C}_{33}\text{H}_{60}\text{O}_6\text{Pr}$ molecules (CAS number 15492-48-5), which are disassociated by electron impact; further impacts sequentially raise the charge state of the ions until the electron beam energy cannot overcome the binding energy of the outermost electron. The combination of negative space-charge potential of the electron beam and voltages applied to the set of hollow electrodes (called drift tubes) trap the HCI inside the central drift tube. By suitably lowering the longitudinal trapping potential caused by the drift tubes, lower ionization states are preferentially evaporated, so that predominantly Pr^{9+} ions remain trapped. Several million of these form a cylindrical cloud with a length of ~ 5 cm and radius of $200\ \mu\text{m}$. Electron-impact excitation of the HCI steadily populates states which then decay along many different fluorescent channels. Spectra in the range from 220 to 550 nm were recorded using a 2-m focal length Czerny Turner type spectrometer equipped with a cooled CCD camera¹⁶. Exploratory searches with a broad entrance slit detected weak lines at reduced resolution. By monitoring the line intensities while scanning the electron beam energy we determined their respective charge state, finding 22 Pr^{9+} lines in total; see Fig. 1c. The charge state identification was made on the basis of a comparison between the estimated electron beam energy at maximum intensity of the lines ($135(10)$ eV), and the predicted

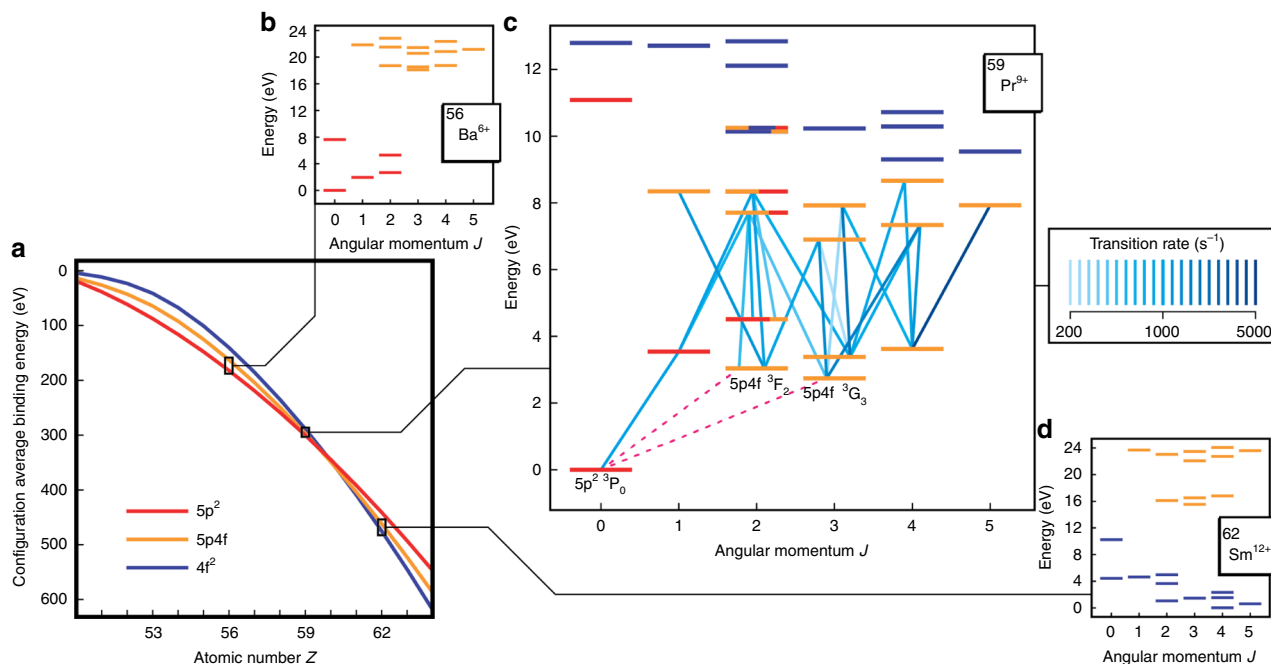


Fig. 1 The $5p - 4f$ orbital crossing and level structures of selected ions along the isoelectronic sequence. **a** Configuration-averaged binding energies for relevant configurations of the Sn-like (50 electron) isoelectronic sequence, as a function of atomic number Z . **b-d** Grotrian diagrams for low-lying levels of the $5p^2$, $5p4f$, and $4f^2$ configurations for $Z = 56, 59$, and 62 , respectively. Pr^{9+} is situated close to the configuration crossing point, and the corresponding diagram shows that inter-configuration optical transitions are allowed. Fig. 1c shows lines that were measured (blue) in the electron beam ion trap (EBIT). Strongly mixed $J = 2$ levels are indicated with multiple colors. We identified potential clock transitions (dashed magenta lines), which are not observable in the EBIT.

ionization energy of Pr^{9+} (147 eV). Here, lines from neighboring charge states appear approximately an order of magnitude weaker compared to their respective maximal intensity. Tentative line identifications were based on wavelengths and line strengths predicted from ab initio calculations. Our Fock-space coupled-cluster¹⁷ calculations were found to reproduce the spectra with average difference (theory – experiment) 14 (28) meV, while our AMBiT¹⁸ calculations (implementing particle-hole configuration interaction with many-body perturbation theory) were accurate to –23 (29) meV (see Methods for further details). Intensity ratios of the lines were compared to predictions by taking into account the wavelength-dependent efficiency of the spectrometer setup and the Pr^{9+} population distribution in the EBIT. The latter was determined from collisional radiative modeling using the Flexible Atomic Code (FAC)¹⁹.

For confirmation and determination of level energies at the part-per-million level, high-resolution measurements were carried out. This revealed their characteristic Zeeman splittings in the $B = 8.000(5)$ T magnetic field at the trap center. Since the only stable Pr isotope ($A = 141$) has a rather large nuclear magnetic moment and a nuclear spin of $I = 5/2$, hyperfine structure (HFS) had to be taken into account to fit the line shapes. We extended the previously employed Zeeman model^{12,16}, to include HFS in the Paschen-Back regime because $\mu_B B \gg A_{\text{HFS}}$ for the involved states. We performed a global fit of the complete dataset to ensure consistent g_j factors extracted from lines connecting to the same fine-structure levels. The good agreement of these with AMBiT predictions conclusively confirmed our line identifications, see Fig. 2, Table 1, and Table 2. Level energies with respect to the $5p^2 \ ^3P_0$ ground state were determined from the wavelengths using the LOPT program²⁰, yielding those necessary to address the $5p4f \ ^3F_2$ and $5p4f \ ^3G_3$ clock states, see Table 1. A prominent example of configuration crossing is given by the $5p4f \ ^3D_1$ and the $5p^2 \ ^3P_2$ levels: their separation of 19 cm^{-1} is comparable to Zeeman splitting in the strong magnetic field. This leads to a pronounced quantum interference of the magnetic substates and to an asymmetry of the emission spectra of the above fine-structure levels when decaying to the $5p4f \ ^3F_2$ state

(see Fig. 2), also seen in e.g. the D lines of alkali metals²¹. The non-diagonal Zeeman matrix element between the near-degenerate fine-structure states, characterizing the magnitude of interference, was extracted by fitting the experimental line shapes, and was found to be in good agreement with AMBiT predictions. The magnetic field strength acts in this setting as a control parameter of quantum interference. In future laser-based high-precision measurements, a much weaker magnetic field will be used. This will minimize interference and enable a better determination of field-free transition energies, and consequently of the clock lines.

Properties of the clock transition. After discovering this orbital crossing and the interesting clock transition, in the following we discuss its properties. Without HFS, the $5p4f \ ^3G_3$ state would decay through a hugely suppressed M3 transition with a lifetime of order 10 million years – a 3 fHz linewidth. However, admixture with the $5p4f \ ^3F_2$ state by hyperfine coupling induces much faster E2 transitions (lifetime ~ years) with widths on the order of nHz, see Fig. 3. In state-of-the-art optical clocks such transitions have been probed⁴ and become accessible in HCI using well-established quantum-logic spectroscopy techniques^{22–24}. The $^3G_3, F = 11/2$ state is decoupled from the ground state but decays to the $F = 9/2$ component with a lifetime of 400 years. For comparison, the $5p4f \ ^3F_2$ E2 transition to the ground state has a much broader linewidth of 6.4 mHz, similar to that of the Al^+ clock^{5,25}.

Blackbody-radiation (BBR) shift is a dominant source of systematic uncertainty in some atomic clocks such as Yb^+ ⁴. However, the static dipole polarisability α_S (to which the BBR shift is proportional) is strongly suppressed in HCI by both the reduced size of the valence electron wave functions and the typically large separations between mixed levels of opposite parity. Together, these lead to a scaling $\alpha_S \sim 1/Z_a^4$ where Z_a is the effective screened charge that the valence electron experiences⁸. Our calculations of the static polarisability for Pr^{9+} yield for the clock state of $\alpha_S = 2.4$ a.u. and confirm the expected suppression. Furthermore, the ground state polarisability is rather similar, so the differential polarisability for the clock transition is $\Delta\alpha_S = 0.05$ a.u., ten times smaller than that of the excellent Al^+ clock transition with $\Delta\alpha_S = 0.43(6)$ a.u.⁵. An atomic clock based on Pr^{9+} would therefore be extremely resilient to BBR even at room temperature.

Beyond their favourable metrological properties, HCI have been suggested for probing variation of fundamental constants due to their high sensitivity to this^{6,7}. Sensitivity to α variation of a transition with frequency ω is usually characterized by the parameter q , defined by the equation

$$\omega = \omega_0 + qx \quad (1)$$

where ω_0 is the frequency at the present-day value of the fine-structure constant α_0 and $x = (\alpha/\alpha_0)^2 - 1$. Calculated q values for Pr^{9+} levels are presented in Table 1, and compared to other proposed transitions in Table 3. The Pr^{9+} M3 clock transition has a sensitivity similar to that of the 467 nm E3 clock transition in Yb^+ , $4f^{14}6s \ ^2S_{1/2} \rightarrow 4f^{13}6s^2 \ ^2F_{7/2}$ ($q = -64000 \text{ cm}^{-1} 26$), but with opposite sign. The sign change can be understood in the single-particle model: the Yb^+ transition is $4f \rightarrow 6s$, while in Pr^{9+} it is $5p \rightarrow 4f$, leading to opposite sign. Comparison of these two clocks would therefore lead to improved limits on α variation and allow control of systematics.

We also investigate the sensitivity of the clock transitions to invariance under local Lorentz transformations. LLI is a fundamental feature of the Standard Model and has been tested

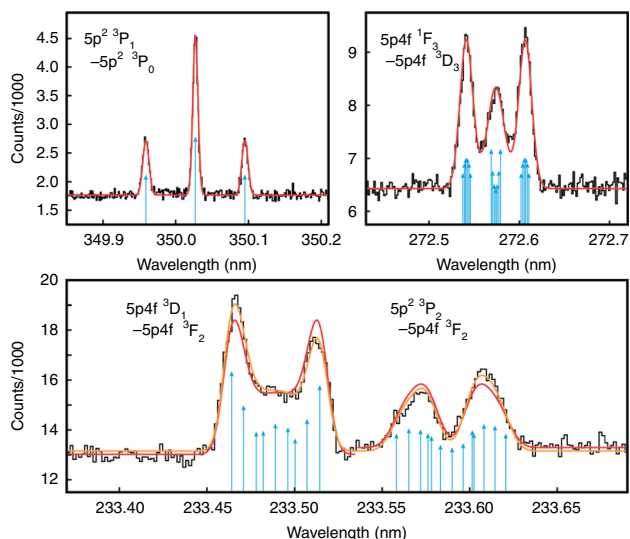


Fig. 2 Spectra of four distinctive Pr^{9+} lines. The measured spectra (black) were fitted with the hyperfine Paschen-Back model shown in red; blue arrows indicate the positions and relative strengths of Zeeman components (collapsing the hyperfine substructure for a clearer presentation). The orange fit in the lower panel includes the effect of Zeeman mixing of the $5p4f \ ^3D_1$ and $5p^2 \ ^3P_2$ levels.

Table 1 Overview and comparison of values relevant to the atomic structure of Pr⁹⁺.

Level	Energy (cm ⁻¹)			g _J				A _{HFS}		q	
	Expt.	AMBIT	ΔE	FSCC	ΔE	4-val ¹⁰	ΔE	Expt.	AMBIT		(GHz)
5p ² ³ P ₀	0	0	0	0	0	0	0	0	0	0	0
5p4f ³ G ₃	22,101.36(5)	21,368	-733	22,248	147	21,895(450)	-206	0.875(2)	0.853	7.771	69,918
5p4f ³ F ₂	24,494.00(5)	23,845	-649	24,525	31	24,199(370)	-295	0.889(5)	0.883	-1.688	64,699
5p4f ³ D ₃	27,287.09(5)	26,372	-915	27,575	288	27,002(570)	-285	1.136(4)	1.145	-3.857	74,073
5p ² ³ P ₁	28,561.063(6)	27,789	-772	28,526	-35	28,436(320)	-125	1.487(3)	1.5	-3.203	39,097
5p4f ³ G _{4a}	29,230.87(6)	28,367	-864	29,482	251	29,343(590)	112	1.130(3)	1.115	5.692	74,358
5p ² ³ D ₂	36,407.48(6)	35,550	-857	35,980	-427	36,217(380)	-190	1.19(1)	1.139	11.004	51,620
5p4f ³ F ₃	55,662.43(5)	54,852	-810	55,737	75	55,220(710)	-442	0.940(2)	0.943	2.568	110,266
5p4f ³ F ₄	59,184.84(5)	58,469	-716	59,393	208			1.158(2)	1.161	2.31	112,108
5p ² ³ F ₂	62,182.14(2)	61,325	-857	62,380	198			1.028(5)	1.054	2.224	101,716
5p4f ³ G ₅	63,924.17(6)	62,788	-1136	64,214	290			1.202(2)	1.2	2.347	113,269
5p4f ¹ F ₃	63,963.57(6)	62,721	-1243	64,379	415			1.197(6)	1.226	0.485	112,004
5p ² ³ P ₂	67,290.97(5)	66,350	-941	67,343	52			1.210(4)	1.207	2.331	98,759
5p4f ³ D ₁	67,309.3(1)	66,429	-880	67,925	616			0.54(1)	0.5	-2.432	110,679
5p4f ³ G _{4b}	69,861.70(8)	68,528	-1334	70,193	331			1.039(4)	1.023	2.62	111,833
4f ² ³ F ₂		79,693		81,801					0.813	1.026	118,508
5p4f ¹ D ₂		80,569		82,657					0.907	1.555	123,702

Measured values are shown in the Expt. columns. Calculated energies and Landé g_J factors of the Pr⁹⁺ states stem from AMBIT, Fock-space coupled-cluster (FSCC), and CI+all-order calculations with four valence electrons (4-val). Magnetic-dipole hyperfine structure constants A_{HFS} and sensitivities to α-variation q were calculated using the AMBIT code

Table 2 Energies and rates of Pr⁹⁺ lines. The measured values (Expt.) include a 1 standard deviation uncertainty given in brackets, they are compared to ab initio theory predictions.

Lower	Upper	Energy (eV)			Rate (s ⁻¹)
		Expt.	AMBIT	FSCC	
5p ² ³ D ₂	5p ² ³ F ₂	3.19563(1)	3.1957	3.2732	
5p4f ³ D ₃	5p4f ³ F ₃	3.51807(2)	3.5311	3.4916	
5p ² ³ P ₀	5p ² ³ P ₁	3.5411202(8)	3.4454	3.5368	1021
5p4f ³ G _{4a}	5p4f ³ F ₄	3.713810(3)	3.7322	3.7085	1086
5p ² ³ D ₂	5p ² ³ P ₂	3.829068(5)	3.8187	3.8885	374
5p4f ³ F ₂	5p4f ³ F ₃	3.864391(3)	3.8444	3.8698	823
5p4f ³ D ₃	5p4f ³ F ₄	3.954826(3)	3.9795	3.9449	675
5p4f ³ G ₃	5p4f ³ F ₃	4.161043(2)	4.1515	4.1521	1342
5p ² ³ P ₁	5p ² ³ F ₂	4.168481(3)	4.1579	4.1974	493
5p4f ³ G _{4a}	5p4f ³ G ₅	4.301421(1)	4.2677	4.3062	4334
5p4f ³ G _{4a}	5p4f ¹ F ₃	4.306314(3)	4.2594	4.3267	640
5p4f ³ D ₃	5p4f ¹ F ₃	4.547299(3)	4.5067	4.5631	1991
5p4f ³ G ₃	5p4f ³ F ₄	4.597753(6)	4.5999	4.6054	1660
5p4f ³ F ₂	5p ² ³ F ₂	4.672740(8)	4.6469	4.6934	483
5p ² ³ P ₁	5p ² ³ P ₂	4.80191(1)	4.7810	4.8127	1060
5p4f ³ D ₃	5p ² ³ P ₂	4.959843(4)	4.9566	4.9306	762
5p4f ³ G ₃	5p ² ³ F ₂	4.969391(7)	4.9540	4.9757	386
5p4f ³ G _{4a}	5p4f ³ G _{4b}	5.037586(9)	4.9793	5.0475	876
5p4f ³ G ₃	5p4f ¹ F ₃	5.19021(2)	5.1271	5.2236	252
5p4f ³ D ₃	5p4f ³ G _{4b}	5.27855(2)	5.2267	5.2840	878
5p4f ³ F ₂	5p ² ³ P ₂	5.30616(2)	5.2699	5.3088	1022
5p4f ³ F ₂	5p4f ³ D ₁	5.30842(2)	5.2797	5.3809	1199

The rate is calculated using theoretical matrix elements from AMBIT and experimental transition frequencies

in all sectors of physics²⁷. While Michelson-Morley experiments verify the isotropy of the speed of light, recent atomic experiments have placed strong limits on LLI-breaking parameters in the electron-photon sector^{28,29}. The sensitivity of transitions for such studies is given by the reduced matrix element of $T^{(2)}$, defined by

$$T_0^{(2)} = c\gamma_0(\mathbf{y} \cdot \mathbf{p} - 3\gamma_z p_z) \quad (2)$$

where c is the speed of light, (γ_0, \mathbf{y}) are Dirac matrices, and \mathbf{p} is the momentum of a bound electron. We find $\langle J||T^{(2)}||J \rangle = 74.2$

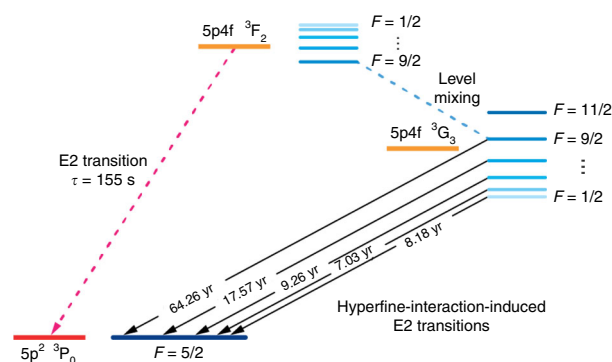


Fig. 3 Schematic level diagram. Shown are the ground and lowest two fine-structure states in Pr⁹⁺ between which the clock transitions take place, energy splittings not to scale. Levels with the same total angular momentum $F = I + J$ are admixed by the magnetic hyperfine interaction, allowing the ³G₃ clock states to decay via E2 transition rather than M3, which would take of order 10 million years to decay.

a.u. for the ³G₃ state, similar in magnitude to the most sensitive Dy and Yb⁺ clock transitions, see Table 3. Again, the sign is opposite to Yb⁺ E3, making their comparison more powerful and improving the control of potential systematic effects. Furthermore, the value compares well with other HCI³⁰.

Proposal for precision laser spectroscopy. Future precision spectroscopy of the clock transitions will require that the internal Pr⁹⁺ state be prepared and detected using quantum-logic protocols in HCI that are sympathetically cooled in a cryogenic Paul trap^{31,32}. Populations calculated using FAC show that a Pr⁹⁺ ion ejected from the EBIT ends up after a few minutes in either the ³P₀ (25%) or ³G₃ state (75%). We propose to employ state-dependent oscillating optical dipole forces (ODF) formed by two counter-propagating laser beams detuned by one of the trapping frequencies of the two-ion crystal with respect to each other. Electronic- and hyperfine-state selectivity may be achieved by tuning the ODF near one of the HCI resonances. If the HCI is in the target state, the ODF exerts an oscillating force onto the HCI. This displaces its motional state, which can be detected efficiently on the co-trapped Be⁺ ion^{23,33}, further enhanced by employing non-classical states of motion³⁴. We estimate an achievable displacement rate of tens of kHz exciting coherent states of motion

Table 3 Predicted sensitivities to physics beyond the Standard Model.

Ion	Ref.	Level	K	$\langle J T^{(2)} J\rangle$
Pr ⁹⁺		5p4f ³ G ₃	6.32	74.2
		5p4f ³ F ₂	5.28	57.8
Ca ⁺	29	3d ² D _{3/2}		7.09 (12)
		3d ² D _{5/2}		9.25 (15)
Yb ⁺	64,65	4f ¹⁴ 5d ² D _{3/2}	1.00	9.96
		4f ¹⁴ 5d ² D _{5/2}	1.03	12.08
Dy	28,65	4f ¹³ 6s ² 2F _{7/2}	-5.95	-135.2
		4f ⁹ 5d6s J = 10	0.77	69.48
		4f ⁹ 5d ² 6s J = 10	2.55	49.73
Hg ⁺	1,65	5d ⁹ 6s ² 2D _{5/2}	-2.94	

The relative sensitivity to variation of the fine-structure constant $K = 2q/\omega$ is given with respect to the ground state, but note that in dysprosium the fractional sensitivity of transitions between the two upper levels is many orders of magnitude higher since these levels are almost degenerate. Sensitivity to local Lorentz invariance is represented with the reduced matrix elements of the $T^{(2)}$ operator, given in atomic units

for realistic parameters of laser radiation at 408 nm detuned by 1 MHz from the $^3P_0 - 5p4f\ ^3F_2$ transition. Similarly, motional excitation rates of a few kHz can be achieved by detuning laser radiation at 452 nm by 10 Hz from the nHz-wide $^3P_0 - ^3G_3$ clock transition. Since the ion is long-lived in both states, we distinguish between the two clock states by detuning the beams forming the ODF to additionally change the magnetic substate²⁴. State selectivity can be provided by the global detuning of the ODF and the unique g -factor of the electronic and hyperfine states. In case the HCl is in one of the excited hyperfine states of 3G_3 , the lowest hyperfine state $F = 1/2$ can be prepared deterministically by driving appropriate microwave π -pulses between F states, followed by detection if the target F state has been reached. The m_F substate is then prepared by driving $\Delta m_F = \pm 1$ states using appropriately detuned Raman laser beams on the red sideband, followed by ground state cooling^{22,24}.

Despite the high resolution of the measured lines, the $^3P_0 - ^3G_3$ clock transition with expected nHz linewidth is only known to within 1.5 GHz. We can improve this by measuring the $^3P_0 - 5p4f\ ^3F_2$ and $^3G_3 - 5p4f\ ^3F_2$ transitions and performing a Ritz combination. The transitions can be found by employing again counter-propagating Raman beams that excite motion inversely proportional to the detuning of the Raman resonance to the electronic transition²³. Using realistic laser parameters similar to above, tuned near the electronic resonance, we estimate that a scan with 10 MHz steps using 10 ms probe pulses can be performed without missing the transition. Assuming that each scan point requires 100 repetitions we can scan the $\pm 2\sigma$ range in ~ 10 min. By reducing the Raman laser power while extending the probe time, the resolution can be enhanced to the sub-MHz level. Once identified, quantum-logic spectroscopy following^{1,22} on the clock transition can commence. Since the linewidth of the transition is significantly narrower compared to the currently best available lasers³⁵, we expect laser-induced ac Stark shifts that need mitigation using hyper-Ramsey spectroscopy or a variant thereof^{36–45}.

Discussion

We have measured optical inter-configuration lines of Pr⁹⁺, finding the $5p - 4f$ orbital crossing, and thereby determined the frequency of the proposed $^3P_0 - ^3G_3$ clock transition with an accuracy sufficient for quantum-logic spectroscopy at ultra-high resolution. Our state-of-the-art calculations agree well with the measurements, thus we used the obtained wave functions to predict the polarizabilities of the levels and their sensitivities to physics beyond the Standard Model. These are crucial steps towards future precision laser spectroscopy of the clock

transition, for which we have also proposed a detailed experimental scheme.

Methods

Line-shape model. In the hyperfine Paschen-Back regime, the energy shift of a fine-structure state's magnetic sublevel in an external magnetic field is given by

$$E_{\text{PB}} = g_J m_J \mu_B B + A_{\text{HFS}} m_J m_I. \quad (3)$$

Hence, a transition between two fine-structure states has multiple components with energies $E_c = E_0 + \Delta E_{\text{PB}}$ with E_0 the transition energy without an external field, and $\Delta E_{\text{PB}} = E'_{\text{PB}} - E_{\text{PB}}$. Here, and in the following, primed symbols differentiate upper states from lower states. Taking into account the Gaussian shape of individual components, the line-shape function is defined as

$$f(E) = \sum_c a_{\Delta m_J} M^2 \exp\left(-\frac{(E - E_c)^2}{2w^2}\right), \quad (4)$$

where the sum is taken overall combinations of upper and lower magnetic sublevels. The factors $a_{\Delta m_J}$ take into account the known efficiencies of the setup for the two perpendicular linear polarizations of the light, and w is the common linewidth, which is determined by the apparatus response and Doppler broadening. The magnetic-dipole matrix elements M are given by

$$M = \langle J, m_J, I, m_I | \mu | J', m'_J, I', m'_I \rangle \\ \propto \delta_{I,I'} \delta_{m_I, m'_I} (J I J' - m_J \Delta m_J m'_I).$$

The large parentheses denotes a Wigner $3j$ -symbol. It follows that $\Delta m_J = m_J - m'_J = 0, \pm 1$. In case of the asymmetric lines, the above $|J, m_J\rangle$ initial fine-structure states were transformed to the eigenstates of the Zeeman Hamiltonian also taking into account non-diagonal coupling.

Equation (4) was fitted to each measured line with the following free parameters: E_c , w , a constant baseline value (noise floor), and overall amplitude. The results for the extracted transition energies are presented in Table 2. The g_J values of all involved states were kept as global fit parameters for the whole dataset of 22 lines. Shot noise and read-out noise were taken into account for the weighting of the data points. The final uncertainties on the transition energies for each line were taken as the square root of its fit uncertainty and calibration uncertainty added in quadrature.

Fock-space coupled-cluster calculations. The Fock-space coupled-cluster (FSCC) calculations of the transition energies were performed within the framework of the projected Dirac-Coulomb-Breit Hamiltonian⁴⁶. In atomic units ($\hbar = m_e = e = 1$),

$$H_{\text{DCB}} = \sum_i h_{\text{D}}(i) + \sum_i \left(\frac{1}{r_{ij}} + B_{ij} \right). \quad (5)$$

Here, h_{D} is the one-electron Dirac Hamiltonian,

$$h_{\text{D}}(i) = c \alpha_i \cdot \mathbf{p}_i + (\beta_i - 1) c^2 + V_{\text{nuc}}(i), \quad (6)$$

α and β are the four-dimensional Dirac matrices and $r_{ij} = |\mathbf{r}_i - \mathbf{r}_j|$. The nuclear potential $V_{\text{nuc}}(i)$ takes into account the finite size of the nucleus, modeled by a uniformly charged sphere⁴⁷. The two-electron term includes the nonrelativistic electron repulsion and the frequency-independent Breit operator,

$$B_{ij} = -\frac{1}{2r_{ij}} \left[\alpha_i \cdot \alpha_j + (\alpha_i \cdot \mathbf{r}_{ij})(\alpha_j \cdot \mathbf{r}_{ij})/r_{ij}^2 \right], \quad (7)$$

and is correct to second order in the fine-structure constant α .

The calculations started from the closed-shell reference [Kr]4d¹⁰5s² configuration of Pr¹¹⁺. In the first stage the relativistic Hartree-Fock equations were solved for this closed-shell reference state, which was subsequently correlated by solving the coupled-cluster equations. We then proceeded to add two electrons, one at a time, recorelating at each stage, to reach the desired valence state of Pr⁹⁺. We were primarily interested in the $5p^2$ and the $5s4f$ configurations of Pr⁹⁺; however, to achieve optimal accuracy we used a large model space, comprised of 4 s , 5 p , 4 d , 5 f , 3 g , 2 h , and 1 i orbitals. The intermediate Hamiltonian method⁴⁸ was employed to facilitate convergence.

The uncontracted universal basis set⁴⁹ was used, composed of even-tempered Gaussian type orbitals, with exponents given by

$$\xi_n = \gamma \delta^{(n-1)}, \quad \gamma = 106\ 111\ 395.371\ 615 \\ \delta = 0.486\ 752\ 256\ 286. \quad (8)$$

The basis set consisted of 37 s , 31 p , 26 d , 21 f , 16 g , 11 h , and 6 i functions; the convergence of the obtained transition energies with respect to the size of the basis set was verified. All the electrons were correlated.

The energy calculations were performed using the Tel-Aviv Relativistic Atomic Fock-Space coupled-cluster code (TRAFS-3C), written by E. Eliav, U. Kaldor and Y. Ishikawa. The final FSCC transition energies were also corrected for the QED contribution, calculated using the AMBiT program.

Polarizabilities. The polarizabilities were also calculated using the Fock-space coupled-cluster method within the finite-field approach^{50,51}. We used the DIRAC17 program package⁵², as the Tel-Aviv program does not allow for addition of external fields. The $v3z$ basis set of Dyall was used⁵³; 20 electrons were correlated and the model space consisted of $5p$ and $4f$ orbitals. These calculations were carried out in the framework of the Dirac-Coulomb Hamiltonian, as the Breit term is not yet implemented in the DIRAC program.

CI+MBPT calculations. Further calculations of energies and transition properties were obtained using the atomic code AMBiT¹⁸. This code implements the particle-hole CI+MBPT formalism⁵⁴, which builds on the combination of configuration interaction and many-body perturbation theory described in ref. ⁵⁵ (see also ref. ⁵⁶). This method also seeks to solve Eqs. (5)–(7), but treats electron correlations in a very different way. Full details may be found in ref. ¹⁸; below we present salient points for the case of Pr^{9+} .

For the current calculations, we start from relativistic Hartree-Fock using the same closed-shell reference configuration used in the FSCC calculations:

$[\text{Kr}]4d^{10}5s^2$. We then create a B-spline basis set in this V^{N-2} potential, including virtual orbitals up to $n = 30$ and $l = 7$. In the particle-hole CI+MBPT formalism the orbitals are divided into filled shells belonging to a frozen core, valence shells both below and above the Fermi level, and virtual orbitals.

The CI space includes single and double excitations from the $5p^2$, $5p4f$, and $4f^2$ (“leading configurations”) up to $8spdf$, including allowing for particle-hole excitations from the $4d$ and $5s$ shells. This gives an extremely large number of configuration state functions (CSFs) for each symmetry, for example the $J = 4$ matrix has size $N = 798134$. To make this problem tractable we use the emu CI method⁵⁷ where the interactions between highly-excited configurations with holes are ignored.

Correlations with the frozen core orbitals (including $4s$, $4p$, $3d$ shells and those below) as well as the remaining virtual orbitals ($n > 8$ or $l > 3$) are treated using second-order MBPT by modifying the one and two-body radial matrix elements⁵⁵. The effective three-body operator $\Sigma^{(3)}$ is applied to each matrix element separately; to reduce computational cost it is included only when at least one of the configurations involved is a leading configuration⁵⁴. Finally, for the energy calculations we include an extrapolation to higher l in the MBPT basis¹⁰ and Lamb shift (QED) corrections^{58–60}.

Diagonalisation of the CI matrix gives energies and many-body wave functions for the low-lying levels in Pr^{9+} . Using these wave functions we have calculated electromagnetic transition matrix elements (and hence transition rates), hyperfine structure, and matrix elements of $T^{(2)}$ (Eq. (2)). For all of these we have included the effects of core polarisation using the relativistic random-phase approximation (see ref. ⁶¹ for relevant formulas). By contrast q values (Eq. (1)) were obtained in the finite-field approach by directly varying α in the code and repeating the energy calculation. In Table 3, the predicted matrix elements and sensitivities are compared to those of other proposed systems and those already under investigation in relevant high-precision experiments.

Lifetime calculations. Direct decay of the $5p4f\ ^3G_3$ clock state to the ground state proceeds as an M3 transition, which is hugely suppressed and would indicate a lifetime of order 10 million years. However, the hyperfine components of the ^{141}Pr clock state have a small admixture of $J = 2$ levels, allowing for decay via a much faster E2 transition. The rate of the hyperfine-interaction-induced decay can be expressed as a generalized E2 transition

$$R_{\text{HFS-E2}} = \frac{1}{15} (\omega\alpha)^5 \frac{A_{\text{HFS-E2}}^2}{2F+1} \quad (9)$$

where F is the quantum number of total angular momentum of the upper state ($F = I + J$) and the amplitude can be expressed as

$$A_{\text{HFS-E2}}(b \rightarrow a) = \sum_n \left[\frac{\langle a | \hat{h}_{\text{HFS}} | n \rangle \langle n | Q^{(2)} | b \rangle}{E_a - E_n} + \frac{\langle b | \hat{h}_{\text{HFS}} | n \rangle \langle n | Q^{(2)} | a \rangle}{E_b - E_n} \right]. \quad (10)$$

Here \hat{h}_{HFS} and $Q^{(2)}$ are the operators of the hyperfine dipole interaction and the electric quadrupole amplitude, respectively. For the clock transition the sum over intermediate states n in Eq. 10 is dominated by the lowest states with $J = 2$: $5p4f\ ^3F_2$ and $5p^2\ ^3P_2$.

MCDF calculations. Transition energies, hyperfine structure coefficients, and g factors were also evaluated in the framework of the MCDF and relativistic CI methods, as implemented in the GRASP2K atomic structure package⁶², and were found to be in reasonable agreement with the experiment on the level of the CI+MBPT results. As a first step, an MCDF calculation was performed, with the active space of one- and two-electron exchanges ranging from the $5s$, $5p$, and $4f$ spectroscopic orbitals up to $8f$. In the second step, the active space was extended to also include the $4d$ orbitals for a better account of core polarisation effects, and CI calculations were performed with the optimized orbitals obtained in the first step. The extension of the active space in the second step has led to 946k jj -coupled configurations. For a more detailed modeling of the spectral line shapes, the non-diagonal matrix elements of the hyperfine and Zeeman interactions⁶³ and mixing coefficients for sublevels of equal magnetic quantum numbers were also evaluated.

Data availability

The data that support the findings of this study are available from the corresponding author upon reasonable request.

Code availability

The AMBiT code is available at <https://github.com/drjuls/AMBiT>¹⁸, the LOPT program at http://cpc.cs.qub.ac.uk/summaries/AEHM_v1_0.html²⁰, the DIRAC17 package at <http://www.diracprogram.org>, and the GRASP2K code at <https://www-amdis.iaea.org/GRASP2K>⁶². The TRAFS-3C code is available upon reasonable request.

Received: 14 June 2019; Accepted: 1 November 2019;

Published online: 11 December 2019

References

- Rosenband, T. et al. Frequency ratio of Al^+ and Hg^+ single-ion optical clocks; metrology at the 17th decimal place. *Science* **319**, 1808–1812 (2008).
- Chou, C. W., Hume, D. B., Koelmeij, J. C. J., Wineland, D. J. & Rosenband, T. Frequency comparison of two high-accuracy Al^+ optical clocks. *Phys. Rev. Lett.* **104**, 070802 (2010).
- Chou, C. W., Hume, D. B., Rosenband, T. & Wineland, D. J. Optical clocks and relativity. *Science* **329**, 1630–1633 (2010).
- Huntemann, N., Sanner, C., Lipphardt, B., Tamm, C. & Peik, E. Single-ion atomic clock with 3×10^{-18} systematic uncertainty. *Phys. Rev. Lett.* **116**, 063001 (2016).
- Brewer, S. M. et al. $^{27}\text{Al}^+$ quantum-logic clock with a systematic uncertainty below $^{27}\text{Al}^+$. *Phys. Rev. Lett.* **123**, 033201 (2019).
- Schiller, S. Hydrogenlike highly charged ions for tests of the time independence of fundamental constants. *Phys. Rev. Lett.* **98**, 180801 (2007).
- Berengut, J. C., Dzuba, V. A. & Flambaum, V. V. Enhanced laboratory sensitivity to variation of the fine-structure constant using highly charged ions. *Phys. Rev. Lett.* **105**, 120801 (2010).
- Berengut, J. C., Dzuba, V. A., Flambaum, V. V. & Ong, A. Highly charged ions with $E1$, $E1$, and $E2$ transitions within laser range. *Phys. Rev. A* **86**, 022517 (2012).
- Safronova, M. S. et al. Highly charged ions for atomic clocks, quantum information, and search for α variation. *Phys. Rev. Lett.* **113**, 030801 (2014).
- Safronova, M. S. et al. Atomic properties of Cd-like and Sn-like ions for the development of frequency standards and search for the variation of the fine-structure constant. *Phys. Rev. A* **90**, 052509 (2014).
- Kozlov, M. G., Safronova, M. S., Crespo López-Urrutia, J. R. & Schmidt, P. O. Highly charged ions: Optical clocks and applications in fundamental physics. *Rev. Mod. Phys.* **90**, 045005 (2018).
- Windberger, A. et al. Identification of the predicted $5s - 4f$ level crossing optical lines with applications to metrology and searches for the variation of fundamental constants. *Phys. Rev. Lett.* **114**, 150801 (2015).
- Murata, S., Nakajima, T., Safronova, M. S., Safronova, U. I. & Nakamura, N. Visible transitions in Ag-like and Cd-like lanthanide ions. *Phys. Rev. A* **96**, 062506 (2017).
- Nakajima, T. et al. Visible spectra of highly charged holmium ions observed with a compact electron beam ion trap. *Nuclear Instruments and Methods in Physics Research Section B: Beam Interactions with Materials and Atoms* **408**, 118–121 (2017).
- Crespo López-Urrutia, J. R., Dorn, A. D., Moshhammer, R. & Ullrich, J. The Freiburg electron beam ion trap/source project FreEBIT. *Physica Scripta* **1999**, 502 (1999).
- Bekker, H. et al. Laboratory precision measurements of optical emissions from coronal iron. *Phys. Rev. A* **98**, 062514 (2018).
- Kaldor, U. & Eliav, E. *High-Accuracy Calculations for Heavy and Super-Heavy Elements*, vol. 31 of *Adv. Quantum Chem.* (Academic Press, 1998).
- Kahl, E. V. & Berengut, J. C. AMBiT: a program for high-precision relativistic atomic structure calculations. *Comput. Phys. Commun.* **238**, 232 (2019).
- Gu, M. F. The flexible atomic code. *Can. J. Phys.* **86**, 675–689 (2008).
- Kramida, A. The program LOPT for least-squares optimization of energy levels. *Comput. Phys. Commun.* **182**, 419–434 (2011).
- Tremblay, P. et al. Absorption profiles of alkali-metal D lines in the presence of a static magnetic field. *Phys. Rev. A* **42**, 2766–2773 (1990).
- Schmidt, P. O. et al. Spectroscopy using quantum logic. *Science* **309**, 749–752 (2005).
- Wolf, F. et al. Non-destructive state detection for quantum logic spectroscopy of molecular ions. *Nature* **530**, 457–460 (2016).
- Chou, C.-W. et al. Preparation and coherent manipulation of pure quantum states of a single molecular ion. *Nature* **545**, 203–207 (2017).
- Rosenband, T. et al. Observation of the $^1S_0 \rightarrow ^3P_0$ clock transition in $^1S_0 \rightarrow ^3P_0$. *Phys. Rev. Lett.* **98**, 220801 (2007).

26. Dzuba, V. A. & Flambaum, V. V. Relativistic corrections to transition frequencies of Ag I, Dy I, Ho I, Yb II, Yb III, Au I, and Hg II and search for variation of the fine-structure constant. *Phys. Rev. A* **77**, 012515 (2008).
27. Kostecký, V. A. & Russell, N. Data tables for Lorentz and CPT violation. *Rev. Mod. Phys.* **83**, 11 (2011).
28. Hohensee, M. A. et al. Limits on violations of Lorentz symmetry and the Einstein equivalence principle using radio-frequency spectroscopy of atomic dysprosium. *Phys. Rev. Lett.* **111**, 050401 (2013).
29. Pruttivarasin, T. et al. Michelson-Morley analogue for electrons using trapped ions to test Lorentz symmetry. *Nature* **517**, 592 (2015).
30. Shaniv, R. et al. New methods for testing Lorentz invariance with atomic systems. *Phys. Rev. Lett.* **120**, 103202 (2018).
31. Schmöger, L. et al. Coulomb crystallization of highly charged ions. *Science* **347**, 1233–1236 (2015).
32. Leopold, T. et al. A cryogenic radio-frequency ion trap for quantum logic spectroscopy of highly charged ions. *Rev. Sci. Instrum.* **90**, 073201 (2019).
33. Hume, D. B. et al. Trapped-ion state detection through coherent motion. *Phys. Rev. Lett.* **107**, 243902 (2011).
34. Wolf, F. et al. Motional Fock states for quantum-enhanced amplitude and phase measurements with trapped ions. *Nat. Commun.* **10**, 2929 (2019).
35. Matei, D. G. et al. 1.5 μm Lasers with Sub-10 mHz Linewidth. *Phys. Rev. Lett.* **118**, 263202 (2017).
36. Yudin, V. I. et al. Hyper-Ramsey spectroscopy of optical clock transitions. *Phys. Rev. A* **82**, 011804 (2010).
37. Huntemann, N. et al. Generalized Ramsey excitation scheme with suppressed light shift. *Phys. Rev. Lett.* **109**, 213002 (2012).
38. Zanon-Willette, T., Yudin, V. I. & Taichenachev, A. V. Generalized hyper-Ramsey resonance with separated oscillating fields. *Phys. Rev. A* **92**, 023416 (2015).
39. Hobson, R. et al. Modified hyper-Ramsey methods for the elimination of probe shifts in optical clocks. *Phys. Rev. A* **93**, 010501 (2016).
40. Zanon-Willette, T., de Clercq, E. & Arimondo, E. Probe light-shift elimination in generalized hyper-Ramsey quantum clocks. *Phys. Rev. A* **93**, 042506 (2016).
41. Yudin, V. I. et al. Generalized autobalanced Ramsey spectroscopy of clock transitions. *Phys. Rev. Appl.* **9**, 054034 (2018).
42. Sanner, C., Huntemann, N., Lange, R., Tamm, C. & Peik, E. Autobalanced Ramsey spectroscopy. *Phys. Rev. Lett.* **120**, 053602 (2018).
43. Beloy, K. Hyper-Ramsey spectroscopy with probe-laser-intensity fluctuations. *Phys. Rev. A* **97**, 031406 (2018).
44. Yudin, V. I. et al. Combined error signal in Ramsey spectroscopy of clock transitions. *N. J. Phys.* **20**, 123016 (2018).
45. Zanon-Willette, T. et al. Composite laser-pulses spectroscopy for high-accuracy optical clocks: a review of recent progress and perspectives. *Rep. Prog. Phys.* **81**, 094401 (2018).
46. Sucher, J. Foundations of the relativistic theory of many-electron atoms. *Phys. Rev. A* **22**, 348–362 (1980).
47. Ishikawa, Y., Baretty, R. & Binning, R. Relativistic Gaussian basis set calculations on one-electron ions with a nucleus of finite extent. *Chem. Phys. Lett.* **121**, 130 (1985).
48. Eliav, E., Vilkas, M. J., Ishikawa, Y. & Kaldor, U. Extrapolated intermediate Hamiltonian coupled-cluster approach: theory and pilot application to electron affinities of alkali atoms. *J. Chem. Phys.* **122**, 224113 (2005).
49. Malli, G. L., DaSilva, A. B. F. & Ishikawa, Y. Universal Gaussian basis set for accurate *ab initio* relativistic Dirac-Fock calculations. *Phys. Rev. A* **47**, 143–146 (1993).
50. Cohen, H. D. Electric-dipole polarizability of atoms by the Hartree-Fock method. ii. the isoelectronic two- and four-electron series. *J. Chem. Phys.* **43**, 3558–3562 (1965).
51. Monkhorst, H. J. Calculation of properties with the coupled-cluster method. *Int. J. Quant. Chem.* **12**, 421–432 (1977).
52. Visscher, L. et al. *DIRAC, a relativistic ab initio electronic structure program, Release DIRAC17*. <http://www.diracprogram.org> (2017).
53. Gomes, A. S. P., Dyall, K. G. & Visscher, L. Relativistic double-zeta, triple-zeta, and quadruple-zeta basis sets for the lanthanides La-Lu. *Theor. Chem. Acc.* **127**, 369–381 (2010).
54. Berengut, J. C. Particle-hole configuration interaction and many-body perturbation theory: application to Hg^+ . *Phys. Rev. A* **94**, 012502 (2016).
55. Dzuba, V. A., Flambaum, V. V. & Kozlov, M. G. Combination of the many-body perturbation theory with the configuration-interaction method. *Phys. Rev. A* **54**, 3948 (1996).
56. Berengut, J. C., Flambaum, V. V. & Kozlov, M. G. Calculation of isotope shifts and relativistic shifts in C I, C II, C III, and C IV. *Phys. Rev. A* **73**, 012504 (2006).
57. Geddes, A. J., Czapski, D. A., Kahl, E. V. & Berengut, J. C. Saturated-configuration-interaction calculations for five-valent Ta and Db. *Phys. Rev. A* **98**, 042508 (2018).
58. Flambaum, V. V. & Ginges, J. S. M. Radiative potential and calculations of QED radiative corrections to energy levels and electromagnetic amplitudes in many-electron atoms. *Phys. Rev. A* **72**, 052115 (2005).
59. Ginges, J. S. M. & Berengut, J. C. QED radiative corrections and many-body effects in atoms: vacuum polarization and binding energy shifts in alkali metals. *J. Phys. B* **49**, 095001 (2016).
60. Ginges, J. S. M. & Berengut, J. C. Atomic many-body effects and Lamb shifts in alkali metals. *Phys. Rev. A* **93**, 052509 (2016).
61. Dzuba, V. A., Berengut, J. C., Ginges, J. S. M. & Flambaum, V. V. Screening of an oscillating external electric field in atoms. *Phys. Rev. A* **98**, 043411 (2018).
62. Jönsson, P., Gaigalas, G., Bieron, J., Fischer, C. F. & Grant, I. New version: GRASP2K relativistic atomic structure package. *Comput. Phys. Commun.* **184**, 2197–2203 (2013).
63. Andersson, M. & Jönsson, P. HFSZEEMAN—a program for computing weak and intermediate field fine and hyperfine structure Zeeman splittings from MCDHF wave functions. *Comput. Phys. Commun.* **178**, 156–170 (2008).
64. Dzuba, V. A. et al. Strongly enhanced effects of Lorentz symmetry violation in entangled Yb^+ ions. *Nat. Phys.* **12**, 465 (2016).
65. Flambaum, V. V. & Dzuba, V. A. Search for variation of the fundamental constants in atomic, molecular, and nuclear spectra. *Can. J. Phys.* **87**, 25–33 (2009).

Acknowledgements

This work is part of and supported by the DFG Collaborative Research Centre SFB 1225 (ISOQUANT). J.C.B. was supported in this work by the Alexander von Humboldt Foundation and the Australian Research Council (DP190100974). A.B. would like to thank the Center for Information Technology of the University of Groningen for providing access to the Peregrine high performance computing cluster and for their technical support. A.B. is grateful for the support of the UNSW Gordon Godfrey fellowship. P.O.S. acknowledges support from DFG, project SCHM2678/5-1, through SFB 1227 (DQ-mat), project B05, and the Cluster of Excellence EXC 2123 (QuantumFrontiers). We acknowledge funding through the Max Planck-RIKEN-PTB Center for Time, Constants and Fundamental Symmetries (TCFS).

Author contributions

J.C.B. and H.B. conceived this work, selected the targeted ion, and wrote the manuscript. H.B. performed the experiment using methods devised by J.R.C.L.U., and developed the Zeeman line fitting scheme. J.C.B. carried out AMBiT calculations, predicted the lifetimes of the clock transitions, and identified with J.R.C.L.U. the Zeeman-induced asymmetry. P.O.S. worked out the QLS scheme. A.B. performed FSCC and polarizability calculations; Z.H. carried out MCDHF calculations and provided input for the asymmetric line modeling. All authors, including C.H.K. and T.P., contributed to the discussions of the results and manuscript.

Competing interests

The authors declare no competing interests.

Additional information

Correspondence and requests for materials should be addressed to J.C.B.

Peer review information *Nature Communications* thanks Mikhail Kozlov and other, anonymous, reviewers for their contributions to the peer review of this work.

Reprints and permission information is available at <http://www.nature.com/reprints>

Publisher's note Springer Nature remains neutral with regard to jurisdictional claims in published maps and institutional affiliations.



Open Access This article is licensed under a Creative Commons Attribution 4.0 International License, which permits use, sharing, adaptation, distribution and reproduction in any medium or format, as long as you give appropriate credit to the original author(s) and the source, provide a link to the Creative Commons license, and indicate if changes were made. The images or other third party material in this article are included in the article's Creative Commons license, unless indicated otherwise in a credit line to the material. If material is not included in the article's Creative Commons license and your intended use is not permitted by statutory regulation or exceeds the permitted use, you will need to obtain permission directly from the copyright holder. To view a copy of this license, visit <http://creativecommons.org/licenses/by/4.0/>.

© The Author(s) 2019